University of Arkansas, Fayetteville

ScholarWorks@UARK

Electrical Engineering Undergraduate Honors Theses

Electrical Engineering

5-2015

Resonant Spectra of Metal Nanotoroids of Various Sizes

Huong Quynh Tran
University of Arkansas, Fayetteville

Follow this and additional works at: http://scholarworks.uark.edu/eleguht

This thesis is approved.

Thesis Co-Advisors:

Prof. Magda El-Shenawee

Prof. Shui-Qing (Fisher) Yu

RESONANT SPECTRA OF METAL NANOTOROIDS OF VARIOUS SIZES

RESONANT SPECTRA OF METAL NANOTOROIDS OF VARIOUS SIZES

An Undergraduate Honors College Thesis

in the

Department of Electrical Engineering
College of Engineering
University of Arkansas
Fayetteville, Arkansas

By

Huong Quynh Tran

28 February 2014

Abstract

Nowadays, the manipulation of light by using metallic nanostructures has wide applications in photonics, optoelectronics and energy conversion. Along with other universities all over the world, the University of Arkansas is researching on nano-antennas' design, fabrication and applications. Current research in Dr. El-Shenawee's Terahertz Imaging and Spectroscopy Computational Electromagnetics Group, has computationally investigated the behaviors of plasmonic nanostructures by using the commercial finite element electromagnetic solver Ansys® HFSS. This work reproduced the previous work of spectral absorption enhancement of infinite and finite arrays of silver and gold nanotoroids with sizes of the inner radii: 13nm – 21nm, while outer radius of 42nm and more on an amorphous silicon absorbing layer. There are three significant factors in modeling this configuration such as surface resolution, optical properties of materials, and boundary conditions. A convergence study was performed on a gold sphere dimer with 40 nm radii and 1 nm gap between spheres. This illustrated that an at least surface resolution of 0.02 nm was needed to provide converging results in an acceptable computational time for conducted simulations. Furthermore, the Lorentz- Drude models for silver and gold were studied to obtain the optical properties. In addition, in order to reduce computation time and memory consumption by reduction of computational domain, the appropriate symmetry boundary conditions were applied.

In this work, three samples of infinite arrays of gold nanotoroids with the sizes of inner radii: 50nm, 60nm and 100nm, respectively, while outer radius of 150nm were simulated as well. These gold nanotoroids were fabricated on glass substrate and then optically characterized by ellipsometry's transmission measurement. The optical characterization was performed in Dr.

Shui-Qing Yu's Applied Nano and Bio Photonics Group. The observed differences between compute simulations and experimental results in shifting resonance frequencies were analyzed.

This thesis is organized as:

Part I is discussing about the finite element method, boundary conditions and Lorentz-Drude Model. Part II involves Lorentz-Drude model for gold and silver, convergence study using HFSS, simulations of infinite silver and gold nanotoroid arrays and ellipsometry transmission measurement on gold nanotoroid arrays. Part III is about conclusions and future research. The Appendix A is providing Matlab codes of Lorentz-Drude model for gold and silver.

Thesis Duplication Release

       I hereby authorize the University of Arkansas Libraries to duplicate this thesis when needed for research and/or scholarship

Agreed_____
               Huong Quynh Tran

Refused_____
               Huong Quynh Tran

Acknowledgements

I would like to thank Dr. El- Shenawee and Dr. Yu, my thesis co-advisors, for their great support and encouragement to help me conduct my undergraduate research. They are my role models when it comes to knowledge, professional and personal characteristics. They have taught me how to perform proper research and how to apply knowledge to research problems. I would also like to thank to the research groups' members, especially Nathan Burford, Amir Ghetmiri and Liang Huang for the HFSS and the Ellipsometry measurement tutorials and samples preparation.

I would like to thank my family for their love and believes. They are always supportive and encouraging for my whole life. For all my friends at the university and also back home, I am grateful to have you as friends. Last but not least, thank God for all blessings.

Table of Contents

List of Figures

List of Tables

I. Introduction

A. Finite Element Method

Generally, electric and magnetic phenomena are described by Maxwell's equations. Moreover, most of electromagnetic work will be involved with fields that are harmonic, time dependence with steady state conditions. In this case, assuming an $e^{j\omega t}$ time dependence, the Maxwell's equations can be written as phasor forms:

$$\nabla \times \overline{H} = j\omega\varepsilon\overline{E} + \sigma\overline{E}$$

$$\nabla \times \overline{E} = -j\omega\mu\overline{H}$$

where $\overline{E}$ and $\overline{H}$ are the phasors of the electric and magnetic fields, σ, ε and μ are conductivity, permittivity and permeability of material, respectively, and ω is angular frequency of incident wave. Those equations can be solved using the finite element method (FEM) that is a numerical technique to find approximate solutions to boundary value problems.

The element in FEM can have one, two, or three dimensional shapes (1D, 2D or 3D). In fact, many problems are truly 3D, and there is no simple way to describe them with lower order geometry. The numerical simulations in this thesis are performed using the commercial Finite Element Method (FEM) Ansys® HFSS. HFSS uses 3D FEM with basic building blocks to discretize the model to conform to arbitrary geometry. The basic building blocks are called as tetrahedra, and those tetrahedra have various shapes at different regions of the model to obtain accuracy solutions. The entire collection of tetrahedra is called a mesh. With appropriate boundary conditions, the differential equations can be represented as a system of equations and solved simultaneously.

Upon discretizing the configuration into tetrahedra and applying the wave excitations, HFSS creates a matrix form to solve those differential equations:

$$[A][x]=[b]$$

where $[A]$ is a defined matrix that is created from the geometry, $[b]$ is a vector representing the excitation and $[x]$ is a variable vector that need to be solved. $[x]$ represents the unknown $\bar{E}$ and $\bar{H}$ in all points of the computational domain. In fact, the value of the H-field or E-field at points inside each tetrahedron is interpolated from the vertices of the tetrahedron. The vertices contain the components of a field that are tangential to the edges of an element. The midpoint of selected edges contains the component of a field that is tangential to the face of an element and normal to the edge.

The generation of the appropriate mesh is the most important process of the FEM. The tetrahedron can be linear with straight edges and planar faces, or it can be non-linear with curved edges and/or curved faces. There is a trade-off among the size of mesh, the desired level of accuracy and the amount of available computing resources. In fact, the solution from using thousands of elements is more accurate than those from using relatively few elements. In order to generate a precise field quantity, each element must cover a region that is small enough for sufficiently interpolated from the nodal values. However, for meshes with a large number of elements, it is necessary for matrix computation to require a significant amount of computing power and memory. Therefore, it is desirable to use a mesh fine enough to obtain an accurate field solution, and it does not overwhelm the memory and processor. Otherwise, high performance computer needs to be used.

In order to produce the optimal mesh, HFSS uses an iterative process, which is an adaptive analysis. This analysis helps the mesh to be automatically refined in critical regions. In

2

the beginning process, HFSS generates an initial mesh following the surface approximation settings. The initial mesh is generated only once before the solution process, but it can be regenerated if the current mesh is unavailable. Moreover, the mesher will automatically repair to recover an accurate mesh for the model, and the repairs will be stored in the solution profile. In addition, if there is any material dependent wavelength, HFSS refines the initial mesh to satisfy lambda refinement. After generation of the resulting mesh, HFSS computes the electromagnetic fields that exist inside the structure when it is excited at the solution frequency. Moreover, HFSS also uses the current finite element to estimate the regions of the domain whose the exact solution has strong errors, then tetrahedra in these regions are refined. After generating the refined mesh, HFSS generates another solution. This is the iterative process, in which HFSS keeps recomputing the error and then performing refinement until the convergence are satisfied or the maximum number of adaptive passes is reached. For a frequency sweep, HFSS solves the problem at the other frequency points without refining the mesh.

HFSS original model surfaces may be planar, cylindrical or conical, toroidal, spherical or splines, and they are called true surfaces, see fig. 1. In order to create a finite element mesh, HFSS divides all true surfaces into triangles, see fig. 2. For planar surfaces, the triangles lie on the model faces, which means that the normal of the true surface and the meshed surface are the same. For non-planar surfaces, the triangles lie a small distance from the true surface. The distance is called the surface deviation that has the same unit as the model. The surface deviation is bigger near the triangle centers and smaller near the triangle vertices. Moreover, HFSS also uses the normal deviation that is measured in degrees to determine the difference between the normal of the curved surface and the corresponding mesh surface. The aspect ratio of triangles is the ratio of circumscribed radius to the in-radius of the triangle. It is unity for an equilateral

triangle and approaches infinity as the triangle becomes thinner. The surface approximation is applied to the initial mesh. For the initial mesh, all the vertices lies on the true surface, but the adaptive meshing adds the vertices to the meshed surfaces, not to the true surfaces.

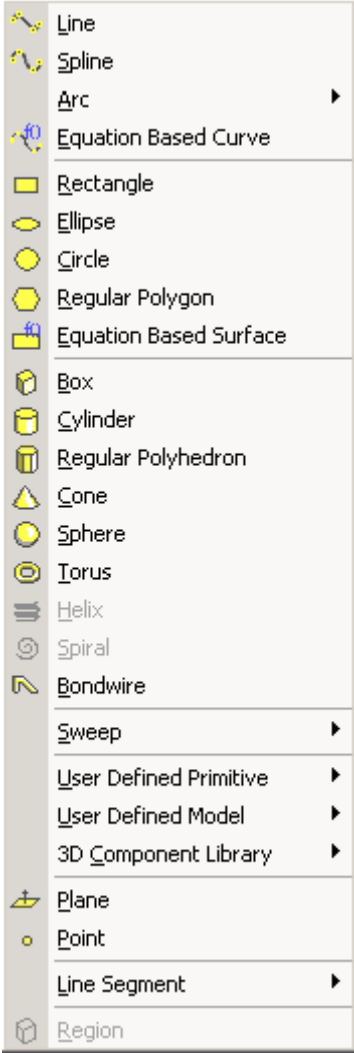|	
Line	
Spline	
Arc	▶
Equation Based Curve	
Rectangle	
Ellipse	
Circle	
Regular Polygon	
Equation Based Surface	
Box	
Cylinder	
Regular Polyhedron	
Cone	
Sphere	
Torus	
Helix	
Spiral	
Bondwire	
Sweep	▶
User Defined Primitive	▶
User Defined Model	▶
3D Component Library	▶
Plane	
Point	
Line Segment	▶
Region	

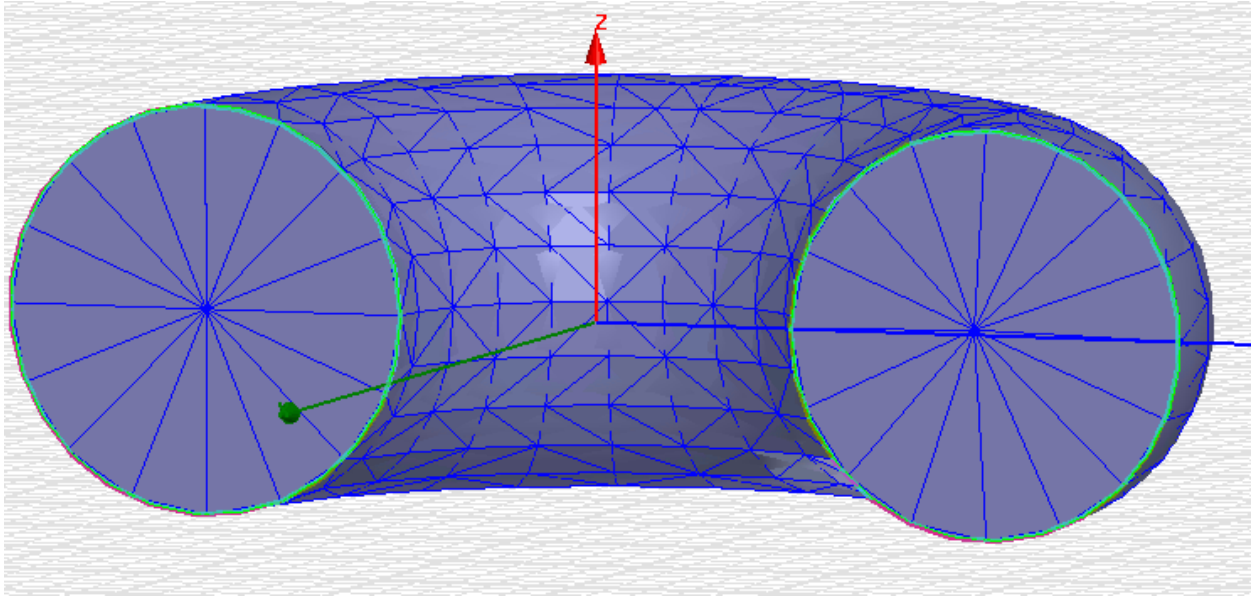**Figure 1. HFSS Original True Surfaces (Software Interface Screen Shot)**

4

Figure 2. HFSS Mesh Operation on ½ Nanotoroid

In HFSS, the problem region and the meshing region are distinguished. The meshing region is the area where an initial mesh is generated, and it also covers the problem region. The problem region is the region in which the solution is generated and the mesh is refined. Hence, it is possible to understand the fact that the meshing region is a domain that happens when generating the initial mesh. The meshing region will enclose the structure, but must be at least 10 times larger than the model. The part of the meshing region that is not object is the background object. Since the background object is defined as a perfect conductor, no solution is generated inside the background. Meanwhile, the problem region is just large enough to include the entire design. Hence, if it is necessary to obtain effects outside of the structure, such as radiated effects, then there is a virtual object that needs to be created to expand the size of the problem region [1].

There are some strengths and some weaknesses for the finite element method. The greatest strength of the method is its generality that is easy to define arbitrary geometries with various levels of resolution. Moreover, this method is unique by automatic mesh refinement. The mesh refinement helps to resolve small details in larger problem space. However, it needs to be

discretized entire volume, and there is a large matrix to compute [2]. Therefore, high performance computation is generally advised to be used.

B. HFSS Boundaries

There are two kinds of models in HFSS, such as open and closed ones. The closed model represents a structure that allows no energy to escape except through an applied port, while the open model represents an electromagnetic model that allows energy to radiate away. As default, HFSS assumes all outer surfaces of the solution space are covered by a perfect electric conductor boundary. Hence, in order to create an open model, it is necessary to specify a boundary on the outer surfaces that will overwrite the default [1].

Perfect E

Perfect E boundaries represent perfectly conducting surfaces in a structure. By default, the electric field is assumed to be normal to all surfaces exposed to the background, which means that the entire structure is surrounded by perfectly conducting walls. In perfect E boundary condition, the final field solution must have the tangential component of the electric field to go to zero, see fig. 3.

It is also possible to assign perfect E boundaries to surfaces within a structure. In order to model the perfectly conducting surface, the perfect E boundaries can be applied. Moreover, the surfaces of all objects that are made by perfectly conducting materials are automatically assigned to be perfect E boundaries [1].
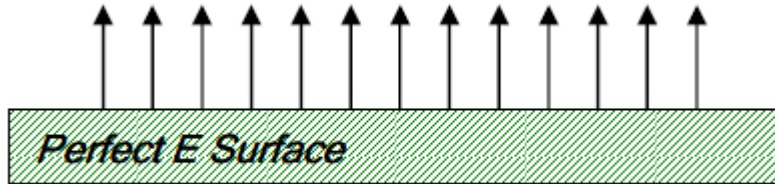
Figure 3. Electric Fields on Perfect E Surface[1]

Perfect H

The perfect H boundary forces the tangential component of the H-field to be the same on both sides of the boundary. For internal planes, this results in a natural boundary through which the field propagates. For planes on the outer surface of the model, this results in a boundary that simulates a perfect magnetic conductor (the tangential component of the H field is zero), see fig. 4.

Those cases in which it is necessary to determine which type of symmetry boundary to use, a perfect E or a perfect H are distinguished based on two points. If the symmetry is such that the E-field is normal to the symmetry plane, then use a perfect E plane. If the symmetry is such that the E-field is tangential to the symmetry plane, then use a perfect H plane [1].

Figure 4. Electric Fields on Perfect H Surface[1]

Radiation

A radiation boundary is created to allow waves to radiate infinitely far into space where it is eventually attenuated. The radiation boundary condition should not produce any unphysical reflection. In other words, the wave is absorbed at the radiation boundary plane, so the system makes the boundary to balloon infinitely far away from the structure. Hence,

7

open space is represented by surfaces that are modeled by radiation boundaries. Energy is allowed to radiate from these boundaries instead of being contained within them. The second-order radiation boundary condition is an approximation of free space. The accuracy of the approximation depends on the distance between the boundary and the object from which the radiation emanates. A radiation surface does not need to be spherical. However, it must be exposed to the background, convex with regard to the radiation source, and located at least one-quarter of a wavelength away from the radiating sources. In some cases, the radiation boundary may be located closer than one-quarter wavelength. Portions of the radiation boundary where little radiated energy is expected can be located closer than one-quarter wavelength [1].
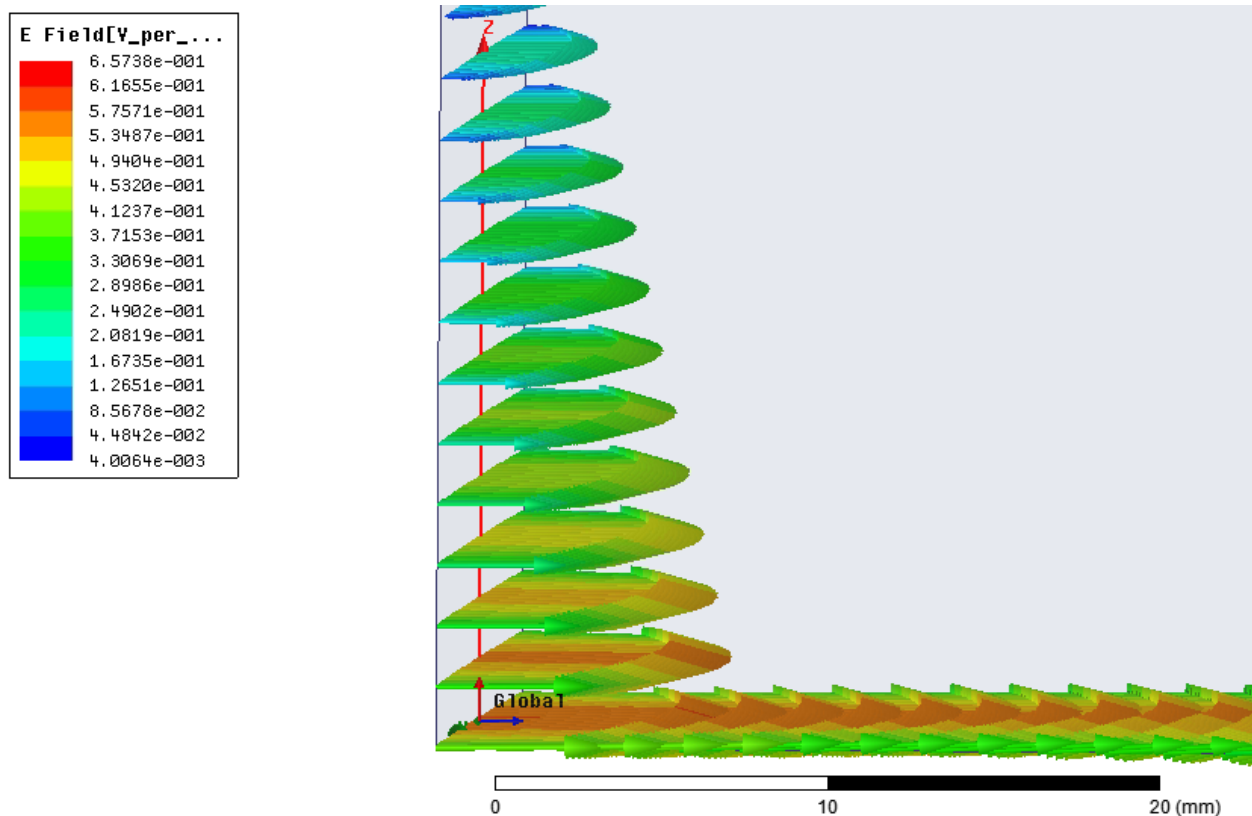

Figure 5. Electric Fields on Perfect E (x-z plane) and Perfect H (x-y plane) Surfaces

C. Lorentz-Drude Model

In this thesis, gold (Au) and silver (Ag) are frequency dependent materials. The optical properties of those materials can be calculated using the hybrid Lorentz-Drude model. The model provides a dielectric function over a wide frequency range.

Lorentz-Drude model:

$$\varepsilon(\omega) = \varepsilon_{r,\infty} + \sum_{k=0}^{K} \frac{f_k \omega_p^2}{\omega_k^2 - \omega^2 + i\omega\Gamma_k}$$

where $\varepsilon_{r,\infty}$ is the optical dielectric constant at infinite frequency (for isotropic plasma-like metals: $\varepsilon_{r,\infty} = 1$) and ω_p is the plasma frequency, while ω_k, f_k, and Γ_p are the resonance frequency, strength and damping frequency, respectively, of each kth resonator. For $k = 0$ and ω_0, the general Lorentz-Drude model simplifies to the Drude model of free electrons. The values of parameters for gold and silver are listed below in Table 1 [12].

Table 1. Parameters for Lorentz - Drude Model [12]

Parameters	Ag	Au
ω_p	9.01	9.03
f_0	0.845	0.760
Γ_0	0.048	0.053
f_1	0.065	0.024
Γ_1	3.886	0.241
ω_1	0.816	0.415
f_2	0.124	0.010
Γ_2	0.452	0.345
ω_2	4.481	0.830
f_3	0.011	0.071
Γ_3	0.065	0.870
ω_3	8.185	2.969
f_4	0.840	0.601
Γ_4	0.916	2.494
ω_4	9.083	4.304
f_5	5.646	4.384
Γ_5	2.419	2.214
ω_5	20.29	13.32

where ω_p, ω_i and Γ_i are in eV. f_i has no units.

II. Approach and Implementation

A. Lorentz-Drude Model for Gold and Silver

It is necessary to perform modeling gold and silver's optical properties because those materials are frequency dependent. In fact, their optical parameters change drastically under high frequency conditions. Hence, the optical properties of silver and gold are modeled by Lorentz-Drude Model [12]. Those models were computed using Matlab. Moreover, in practical, there are measurements of the real and imaginary parts of reflection index to characterize those materials' optical parameters. The results from modeling were plotted together with those experimental data from "Handbook of Optical Constants of Solids" [3] or from Burford [5] to observe their difference. The values of real part of relative permittivity are close together between Lorentz − Drude Model and Experimental Data, while the loss tangent values are different in the range of high frequency (when wavelength is less than 300 nm). In this thesis, the desire spectrum range is from 400 nm to 900 nm. In this range, the complex permittivity from Lorentz-Drude model is close to experimental data for both gold and silver. The Lorentz-Drude model for gold was used to set parameters when configuring the gold material in the case of convergence study using HFSS (see section 2.2). For other simulations of infinite nanotoroid arrays (see section 2.3 and 2.4), the measured data from Burford [5] were used.
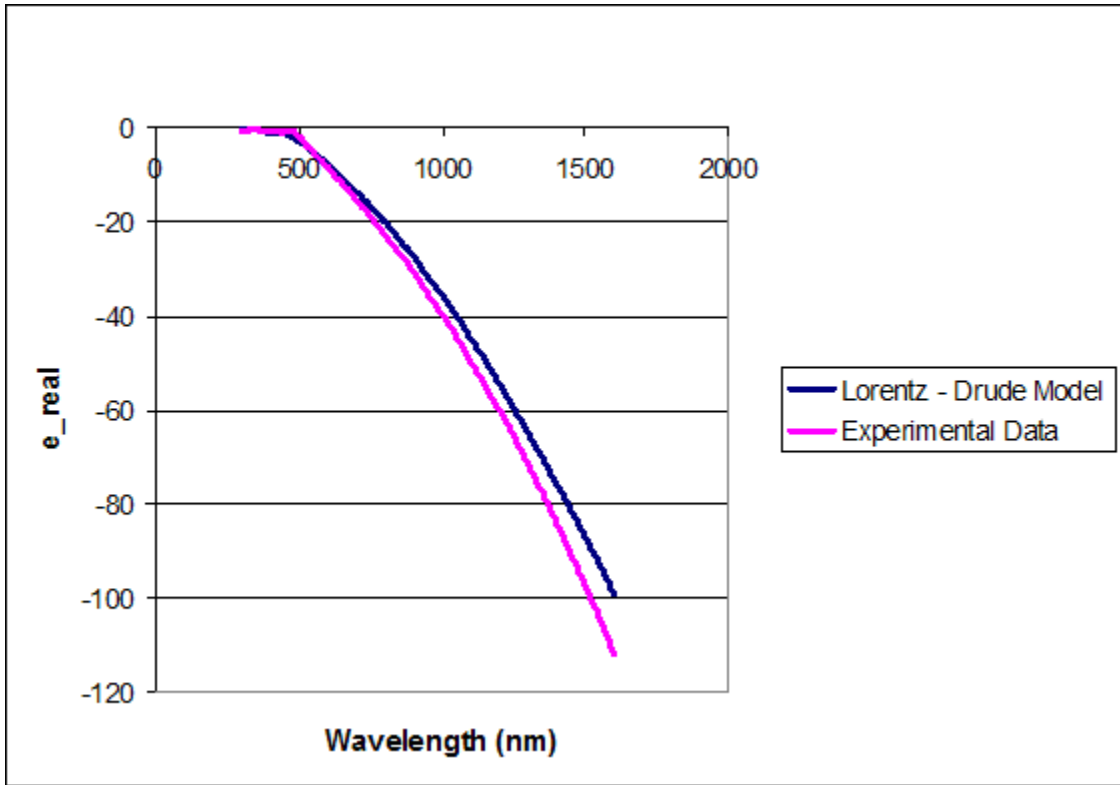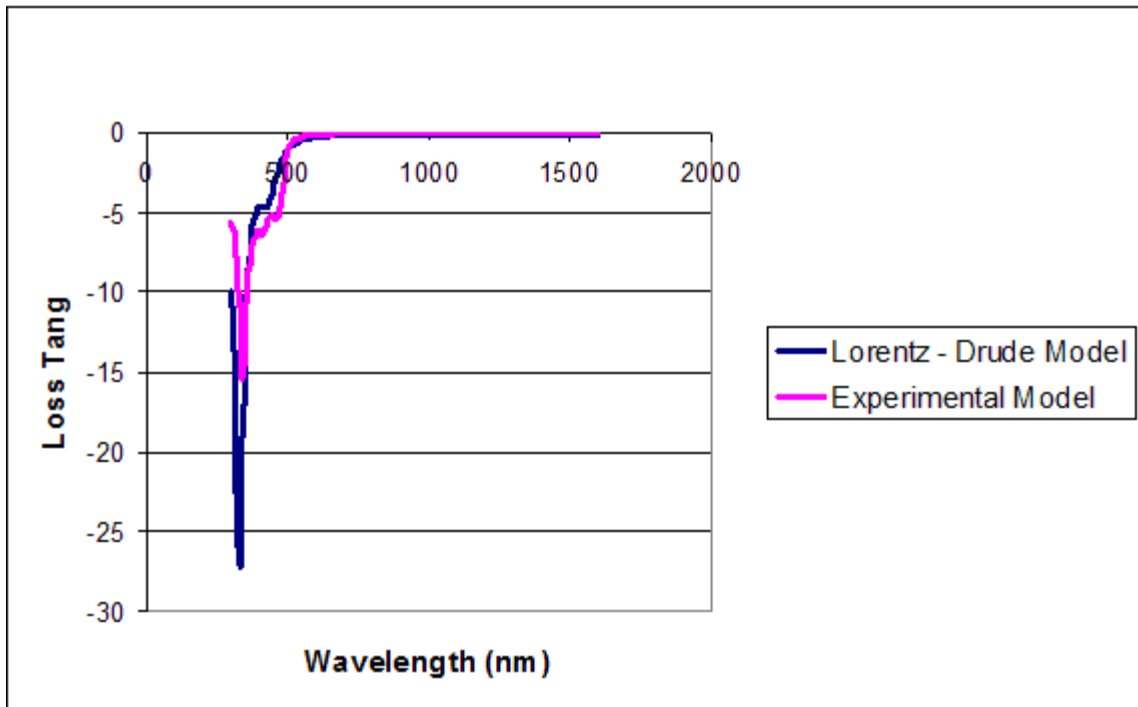
Figure 6. Gold's Real Part of Permittivity
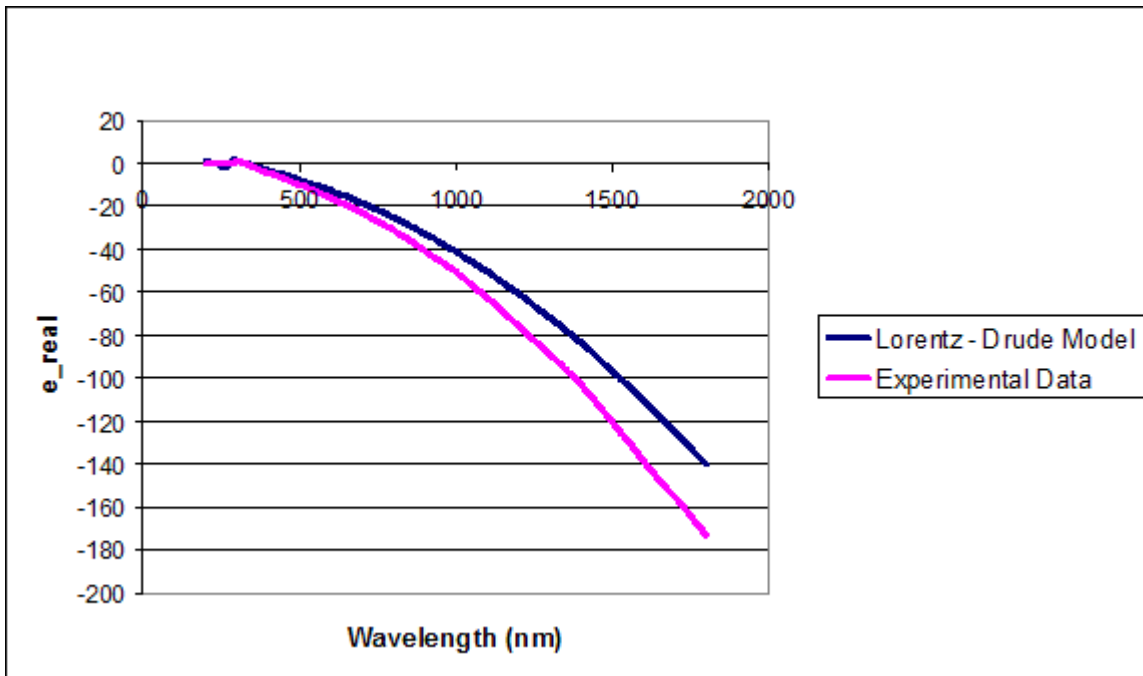

Figure 7. Gold's Loss Tangent

Figure 8. Silver's Real Part of Relative Permittivity
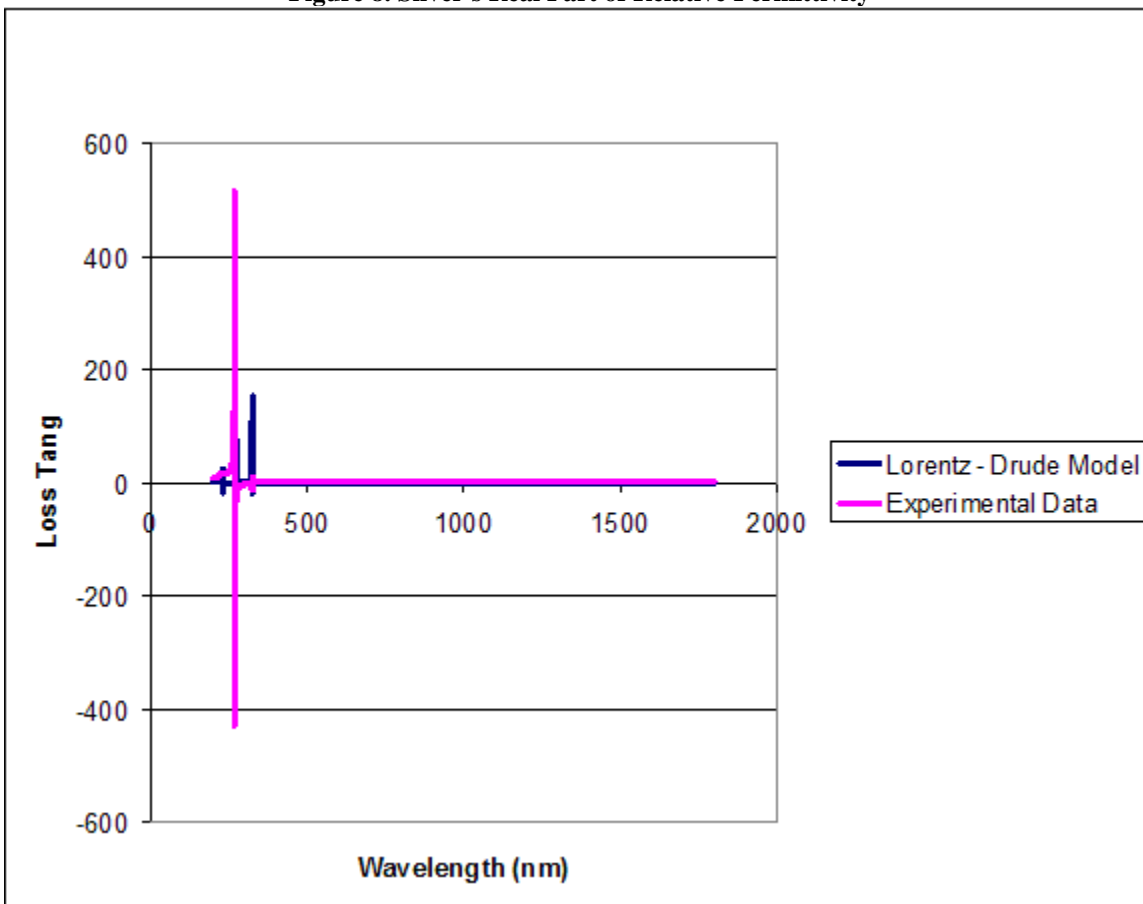

Figure 9. Silver's Loss Tangent

13

B. Convergence Study using HFSS

Procedure

To obtain the appropriate surface resolution with considerations of affordable computational time and of reliable results, there was a convergence study with HFSS applying on the dime sphere with radius of 80 nm and 1 nm gap between spheres. The computational domain was the air box, whose dimensions were 400 nm x 400 nm x 800 nm, see fig. 10. The air box had its centre at the origin. Its length lied on the direction that parallels with *y*-direction, while its width lied on the one that parallels with *x*-direction. Its height paralleled with *z*-direction. To reduce computational domain to 400nm x 200nm x 400nm, it was necessary to apply appropriate boundaries [4]. There were three significant boundaries that were used in this setup such as E symmetry, H symmetry and radiation boundaries. Those symmetry boundaries helped to reduce the computational domain to one forth of the original one. Based on how to set up the excitation plane wave, the symmetry boundaries were applied properly.

In this case, $\vec{E}_0(0, 1V/m, 0)$ and $k_0(1, 0, 0)$, which means that the wave propagated in positive x-direction, were set as how the excitation wave propagates. E symmetry made the tangent component of the electric field become zero, so the E symmetry boundary was applied on the intersection between one face of the air box and the x-z plane. Moreover, H symmetry let the electric field to be parallel, so the H symmetry boundary was applied on one face of the air box that intersects with the x-y plane. Other faces of the computational domain were set as radiation boundaries [1], [4]. The receiver was placed at the origin that was the central point of the gap between the spheres to get the maximum radiated power, and

14

it was a near field measurement for the fact that HFSS near field region is the region closest to the source [1]. The gold material was configured using data that are obtained from Lorentz-Drude model.

The goal of this convergence study was to obtain accuracy resonant wavelength of the dime sphere by changing the surface resolution. Moreover, another factor that was also significant to be considered for simulation was the number of tetrahedra of the model because they indicated the computational time and memory for the required solver.
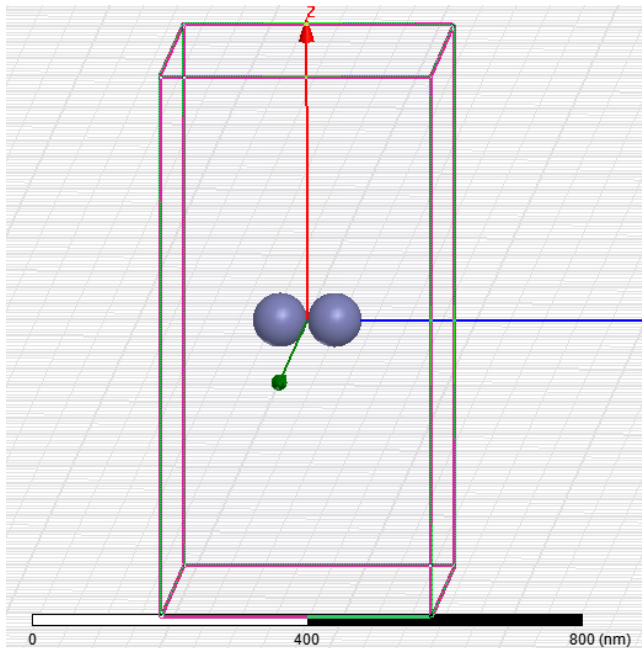

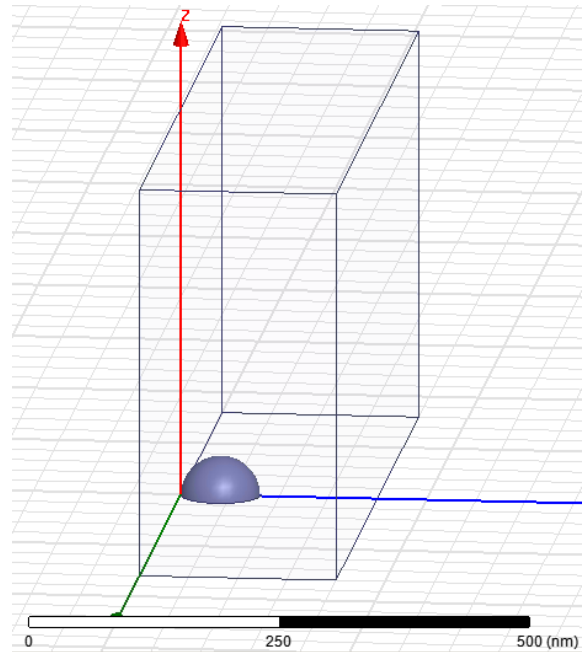**Figure 10. The Gold Sphere Dimer for HFSS Convergence Study**

Figure 11. The HFSS Configuration of the Gold Sphere Dimer after Applying Appropriate Boundaries

Numerical Results

Following the convergence procedure in Burford [5], the influence of surface resolution to the solution was showed in Table 2 and Fig. 12. The recorded results were the

15

number of tetrahedra of the model, RAM, computational time and the magnitude of electrical field curves from the measurement.

Table 2. Convergence Study of HFSS

Surface Resolution (nm)	Number of Tetrahedra of the Air Box	Number of Tetrahedra of the Gold Sphere	Required Memory of the Solver (MB)	Time for Matrix Solution (s)
1.0	1766	871	82.4	13
0.5	2169	1083	96.7	18
0.1	4023	2632	175	20
0.05	7060	5452	333	54
0.02	12238	11207	577	59
0.01	23694	21658	1080	144
0.008	29009	27583	1420	295

Discussion of Results

Upon observing the magnitude of the electrical field in fig. 12, the resonance of the sphere dimer in this case is found at 632 nm, which agrees with Hoffman *et al.* results in [4]. With small surface approximation values, the results converge to the accuracy wavelength. However, it is also found that the more precise the surface resolution is, the larger the memory requirement is. In fact, the surface resolution determines the number of tetrahedra that affect the memory and time for matrix solution. In both experiences, Hoffman *et al.* [4] and this thesis, the curves at surface resolution of 0.02 nm are close to the ones at the resolution of 0.01 nm. However, the number of tetrahedra in 0.01 nm surface resolution is twice larger than the number of the tetrahedral in 0.02 nm surface resolution. Hence, after convergence study above, the surface resolution of 0.02nm which provides the accuracy result in acceptable computation time is used for all later simulations.
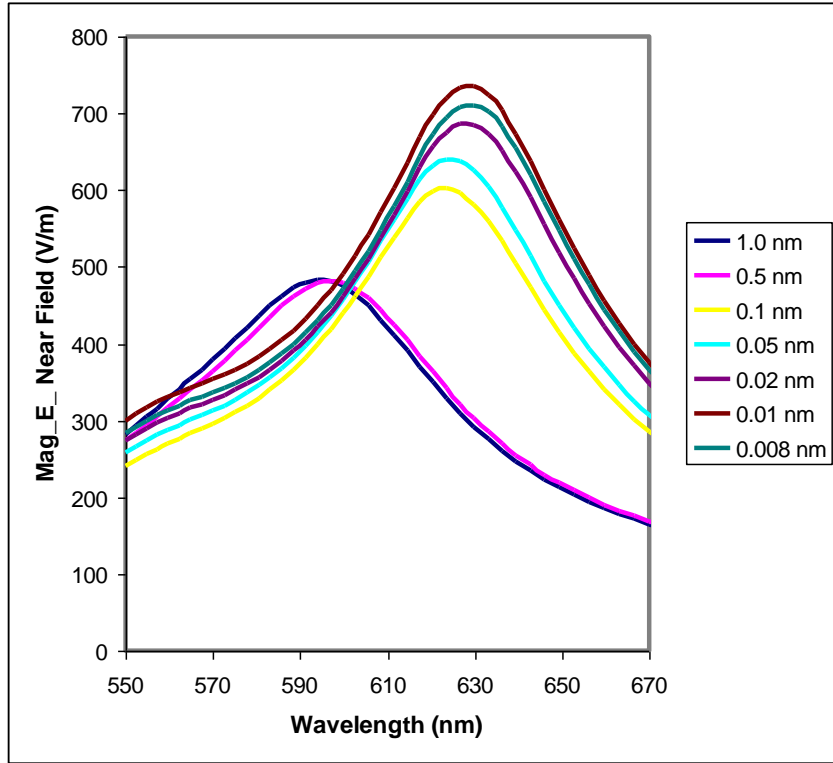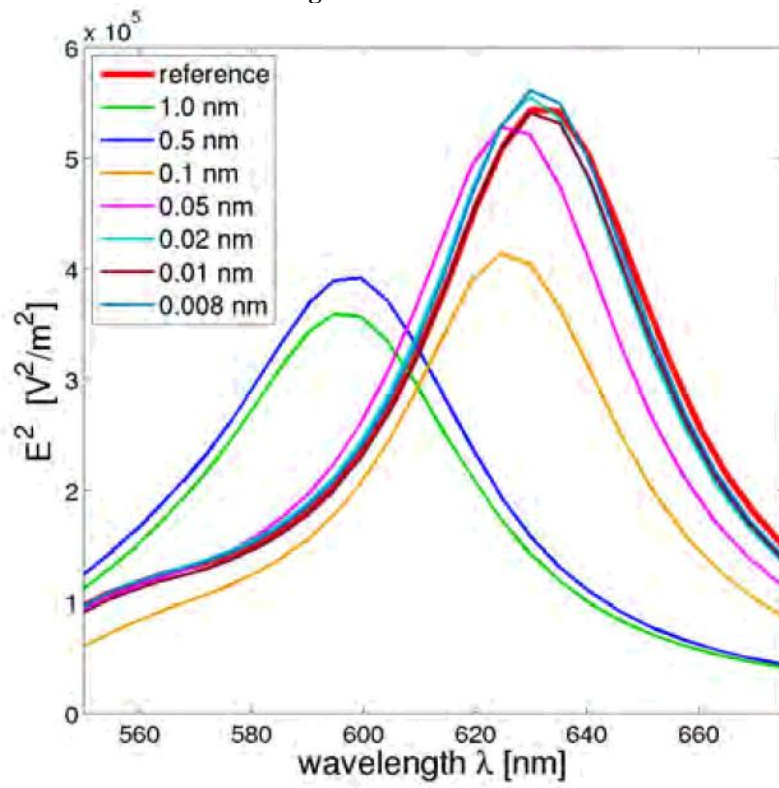
Figure 12. This work

Figure 13. Hoffman *et al.* [4]

C. Simulation of Infinite Silver Nanotoroid Arrays on Armophous Silicon Layer

Procedure

Spectral absorption enhancement of infinite square arrays of silver nanotoroids with sizes of the inner radii: 13 nm, 15 nm and 21 nm, respectively, while outer radius of 42 nm on an amorphous silicon absorbing layer was observed. The a-Si layer had thickness of 500 nm. The silver and a-Si parameters were from Burford thesis' measured data [5]. The spacing from each nanotoroid's centre to other's one was 900 nm. $\vec{E}_0(1V/m, 0, 0)$ and $k_0(0, 0, -1)$, which means that the wave propagated in negative z-direction, were excitation vectors. This case was selected to reproduce the results in Burford [5].

Again, the appropriate boundaries were applied to reduce the computational domain. The two same kind boundary symmetries (perfect E or perfect H) were placed face to face to get the mirror effect [5], [6]. Each perfect E plane and each perfect H plane mirrored a quarter of nanotoroid to become a full size of nanotoroid, while the other perfect E plane and the other perfect H plane helped to clone each nanotoroid to four nanotoroids around [5], [6]. The perfect E boundaries were applied on y-z plane and another plane that was parallel with y-z plane, while the perfect H boundaries were on x-z plane and another plane that was parallel with x-z plane. The other faces of the computational domain were radiation boundaries.

In addition, it was significant to determine step count when sweeping the frequency to observe the resonant spectra. In fact, the step size needed to be small enough to not overstep the peak because the peak was thin. However, it costed the computational time with small steps. Hence, in this case, there were 500 step counts that were performed.
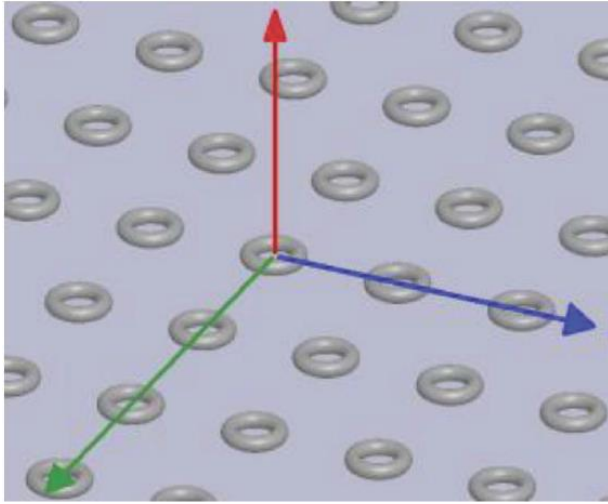
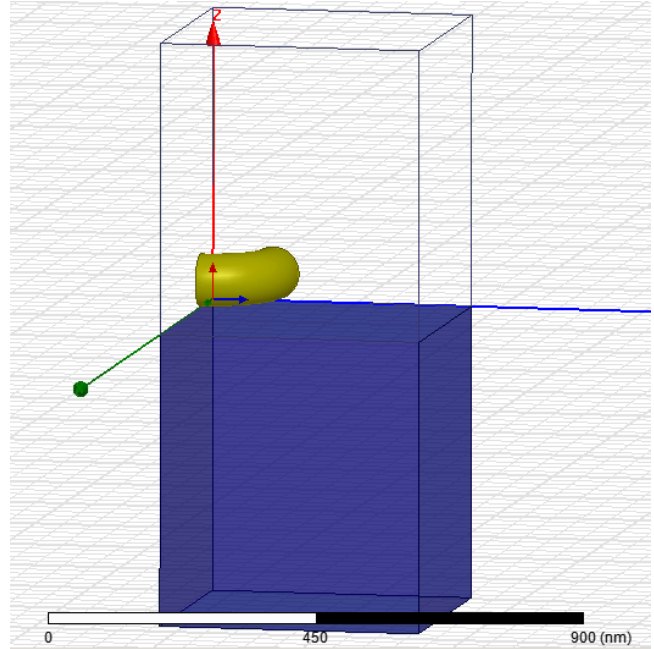**Figure 14. The Infinite Square Arrays of Silver Nanotoroids [5]**

Figure 15. The HFSS Configuration of those Infinite Square Arrays after Applying Appropriate Boundaries [5],[6]
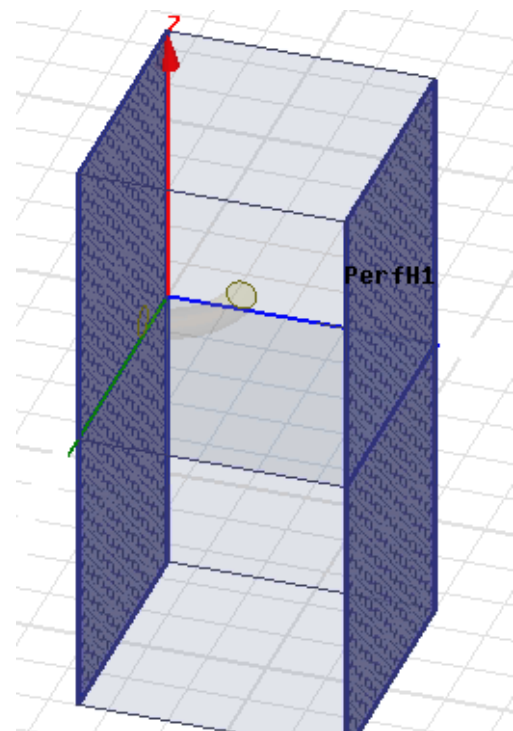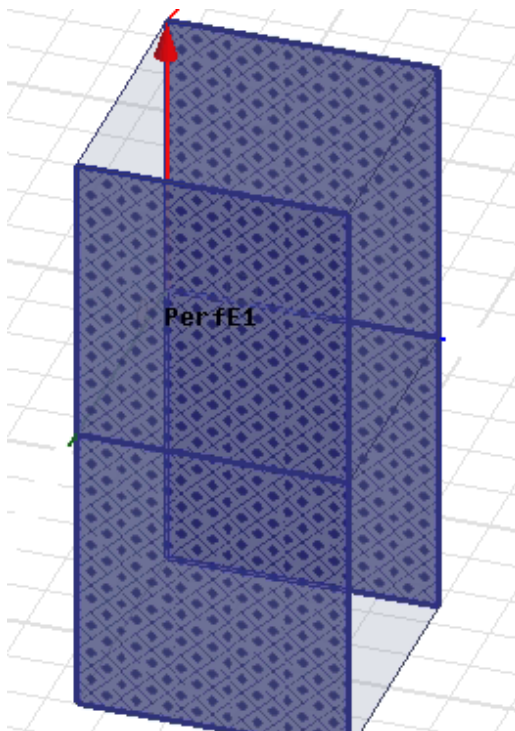
Figure 16. Applied Perfect E and Perfect H Symmetries [5],[6]

Furthermore, it was found that the nanotoroids should be 2 nm floating above the a-Si-layer to get the proper model [6]. The enhancement factor was calculated as the following equation [5]:

$$EF(\lambda) = \frac{\iiint \sigma \left| \vec{E}_{with\,Nanoparticles} \right|^2 dV_{Si}}{\iiint \sigma \left| \vec{E}_{without\,Nanoparticles} \right|^2 dV_{Si}}$$

Results

Figure 17. Resonant Spectra of Silver Nanotoroids

Figure 18. Burford [5]

Discussion of Results

The obtained resonant peaks in this work are located at $\lambda = 630$, 670 and 845 nm for $R_{in} = 13$, 15 and 21nm, respectively, while Burford's resonant peaks in [5] occurs at $\lambda = 652$, 682 and 820 nm. However, in bo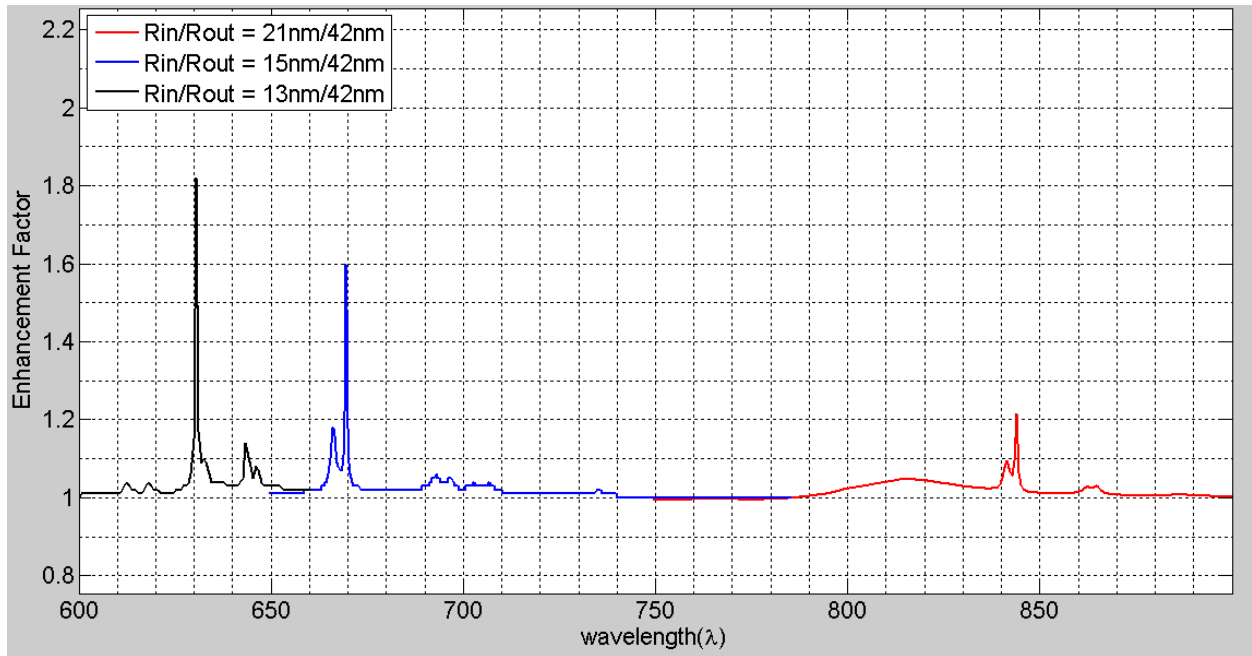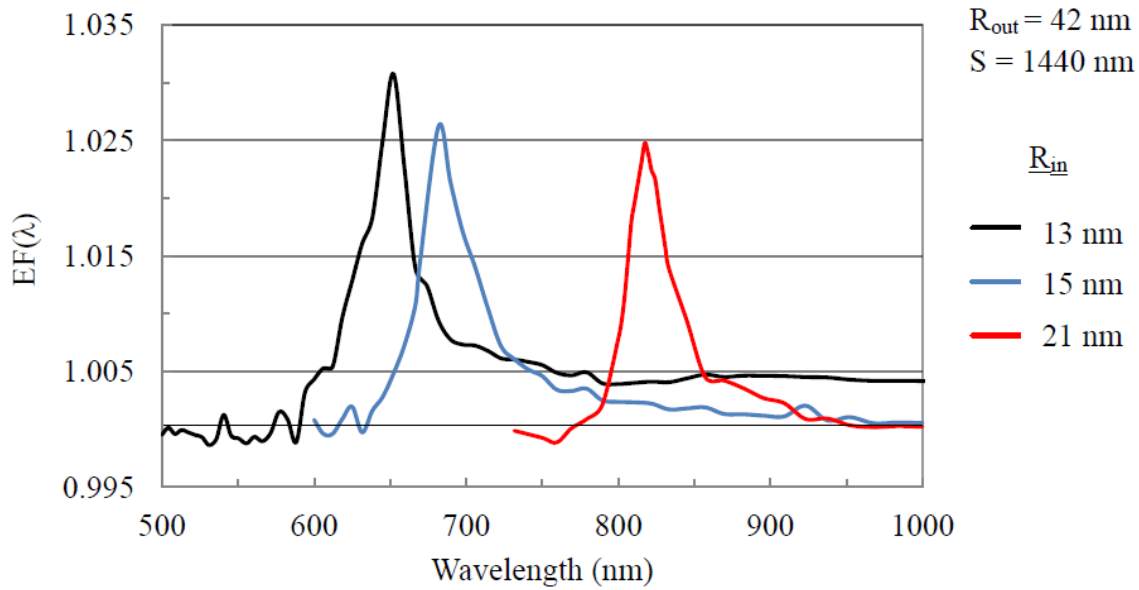th presentations, the value of enhancement factor reduces when the inner radius increases. Moreover, by Mary *et al.* [7], peak scattering by the single Au nanotoroid is shifted to longer wavelengths, and the amplitude of the scattering reduces as well. This work did not perform the converged study for frequency solutions on the high performance computer, while Burford did in [5], and the separation distance between nanotoroids was smaller than Burford's configuration in [5].

D. Simulation of Infinite Gold Nanotoroid Arrays

Other simulations were performed on the gold nanotoroid arrays whose inner radii: 50nm, 60nm and 100nm, respectively, while outer radius of 150nm. The computational

domain was the air box, 900nm x 900nm x 1000nm. The spacing from each nanotoroid's centre to other's one was 900 nm. $\vec{E}_0(1V/m, 0, 0)$ and $k_0(0, 0, -1)$, which means the wave propagated in negative-z direction, were excitation vectors. The gold parameters were from the measured data in Burford [5].

Similarly to the case of silver nanotoroids, the appropriate boundary conditions were applied to reduce the computational domain. The perfect E boundaries were applied on y-z plane and another plane that was parallel with y-z plane, while the perfect H boundaries were on x-z plane and another plane that was parallel with x-z plane. The other faces of the computational domain were radiation boundaries.

Again, it was significant to determine step count when sweeping the frequency to observe the resonant spectra because the solution frequency was determined from the step count. However, it costed the computational time with small steps. Hence, in this case, there were 500 step counts that were performed.

The obtained results are showed in fig. 19. They are in the desire range of wavelength that is from 450nm to 850nm, and the recorded data are their radiated power. The resonances of each sample involve two peaks with different magnitudes, called Fano-like feature. The Fano resonance feature happens when there is interference between scattering fields. The interaction effects happens when the separation distance between nanotoroids is not large enough [14]. There is a situation in which all three samples are put near to each other. In fact, when measuring the real samples of those gold nanotoroids, the fabricated samples are close to each other on the glass substrate. The total field scattered a multi-nanotoroid cluster can be represented as a superposition of individual fields scattered from each sphere [15].

Hence, the summation of all curves was presented to supply the information about the resonance.
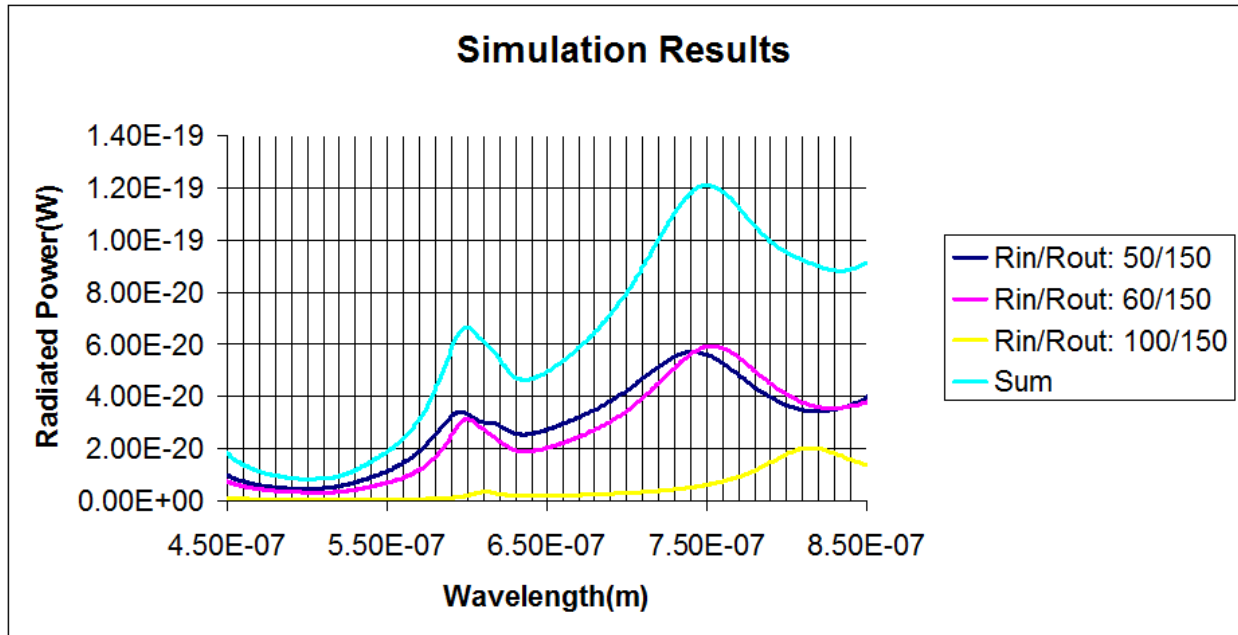

Figure 19. Resonant Spectra of Gold Nanotoroids in Air

E. Ellipsometry's Transmission Measurement on Gold Nanotoroid Arrays

Procedure

Those gold nanotoroids were fabricated on glass substrate[1]. The whole fabrication process started from glass substrate. After 2% 495K PMMA coating (80nm) and baking at 180 degree for 2 minutes, 5nm thick Chromium was deposited as anti-changing layer. The sample then was loaded into e-beam chamber for exposure. Before resist developing, the Chromium layer was removed in we etchant. The developing process was 35 seconds immersion in mixed solution (MIBK:IPA = 1:3). With followed metal deposition and lift-off, the nanotoroid arrays were formed. The geometrical arranges of those arrays are shown in

---

[1] Performed by Liang Huang

figures below. Patterns of d1, d2 and d3 had 1000 x 1000 nanotoroids whose inner radii were 50nm, 60nm and 100nm, respectively.

Moreover, those samples were optically characterized by ellipsometry's transmission measurement. The measurement was performed following these steps:

- Calibrate with the small reference sample :
  - o Mount the small reference sample on.
  - o Put the alignment probe on.
  - o Use the software's align sample function.
- Calibrate the whole system:
  - o Use the software's calibration function.
- Monitor if the light focuses on the position as same as the square on the camera:
  - o Take the reference sample off, and mount the square sample on with the shiny side up.
  - o Use the software's align sample function again.
  - o Switch the sample to the rough side.
  - o On the camera monitor software, close the show function to not see the white square on the camera anymore.
  - o Turn off the light; it should be seen as the purple dot on the camera monitor as well as on the square sample.
  - o On the camera monitor, choose the show function to see the white square, and move the white square to the position that covers the signal.
- Real Sample Measurement:
  - o Take off the square sample, and mount the real sample on.

- o Let the white square on the camera monitor onto the sample.

- o Align sample.

- o Choose the software's R&T function.

- o Choose baseline only.

- o Choose pT, sT and uT.

- o Set the angle from 90 to 90 degree.

- o Save baseline, push the sample holder back to measure directly from input to output through air medium. After finishing this step, the software automatically normalizes the data with the baseline to get the transmission coefficient to be smaller than 1.

- o Let the holder back to original position.

- o Choose R& T again.

- o Choose data only.

- o Choose pT, sT and uT again.

- o Set the angle from 0 to 0 degree. Run the softwave, and get the data.

The quality of the pattern d2's fabricated sample is not qualified. In fact, the expected inner radius for pattern d2 is 60 nm, but in the real sample, it obtains as 53 nm only. It is significantly sensitive in case of changing the sizes of the nanotoroids, which means that there is a big shift in wavelength comparing with small variation of the size of nanotoroids. It will lead the measured result to shift in the desire spectrum.

Figure 21. Pattern d1's Zoom in Nanotoroid (Inner Diameter/ Outer Diameter: 102/302nm)
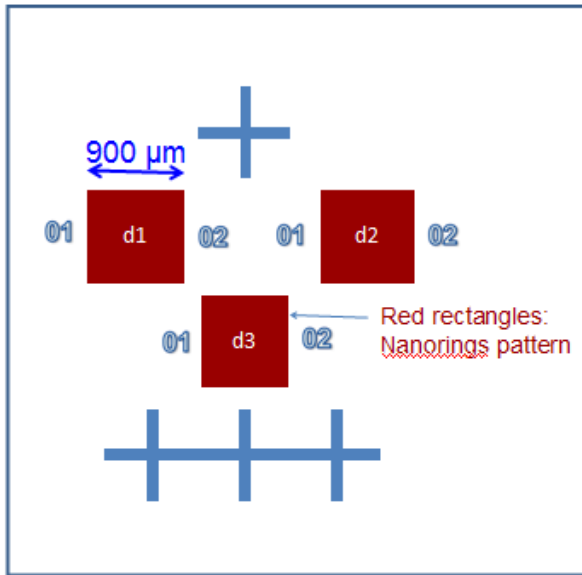
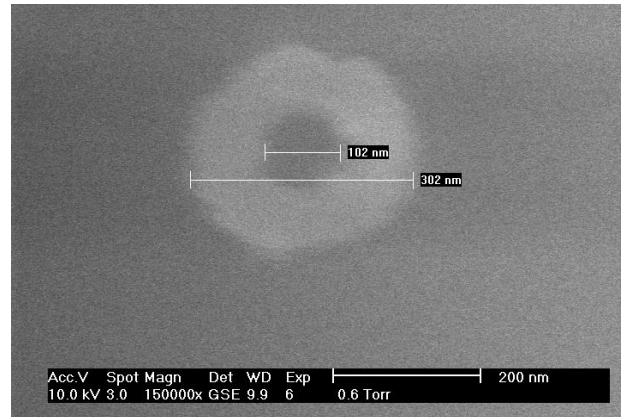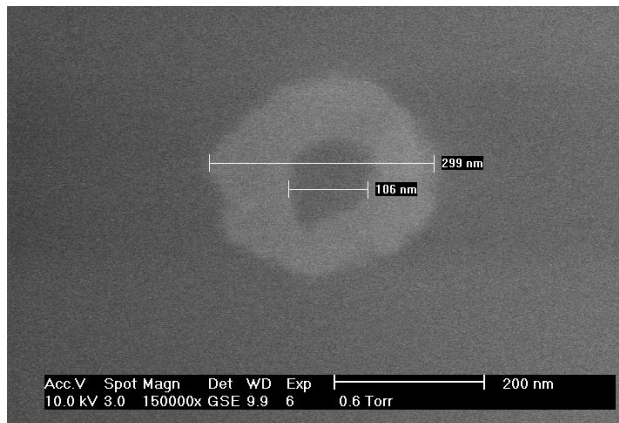**Figure 20. Nano rings CAD design[1]**

Figure 22. Pattern d2's Zoom in Nanotoroid (Inner Diameter/ Outer Diameter: 106/299nm)

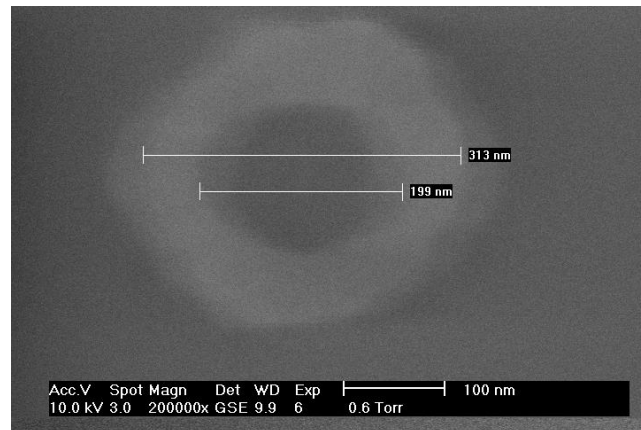**Figure 23. Pattern d3's Zoom in Nanotoroid (Inner Diameter/Outer Diameter: 199/313nm)**

---

[1] Performed by Liang Huang

Results
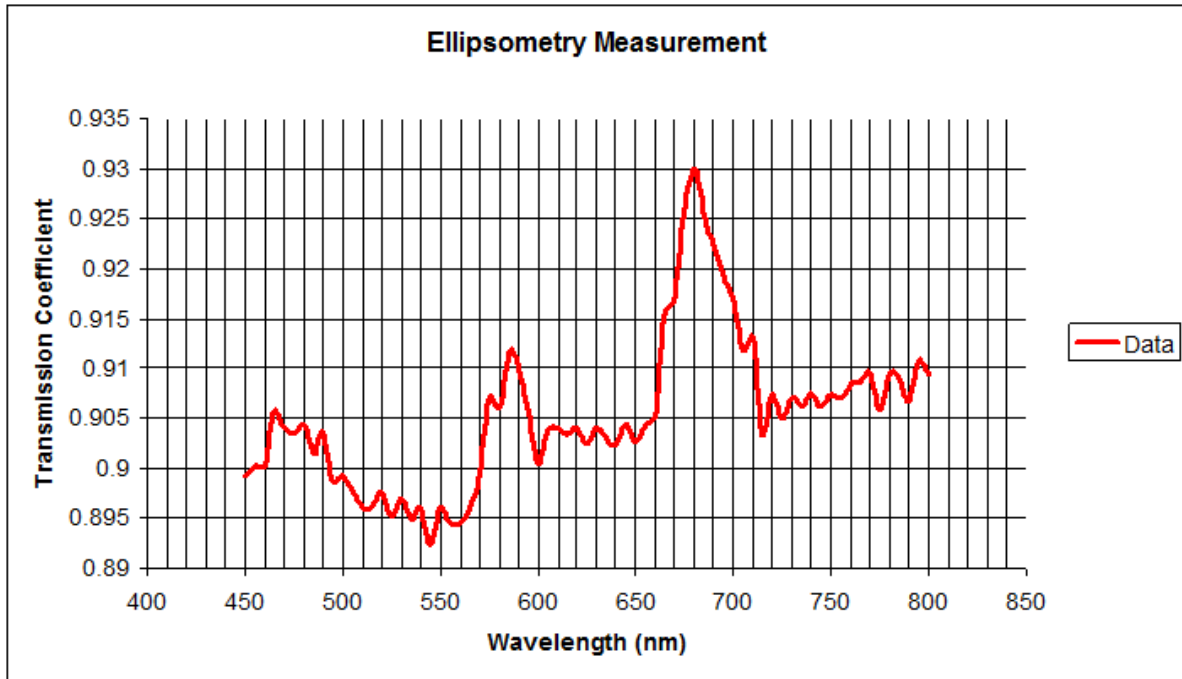
Figure 24. Ellipsometry's Transmission Measurement Performing on Gold Nanotoroids for Normal Incidence Light (0 degree)

Discussion of Results

The measurement's result is slightly different than the simulations' ones. Firstly, the measurement is performed without using the focusing probes, which means that the light shines over all three samples. Hence, the curve here will represent the total behavior of three samples together. Moreover, the three patterns are fabricated at positions which are so close to each other, their scattering field will interfere each other. In addition, the glass substrate's characteristics also affects to the experimental result, while the simulation is performed on those nanotoroids by themselves without the glass substrate.

In the simulation, two peaks happen at the wavelength of 600 nm and 750 nm, respectively, while in the fabricated samples, their peaks happen at the wavelength of 585 nm and 680 nm. It leads to the observation that the presence of glass substrate is the reason to shift the wavelength to lower values. Moreover, the simulation's peaks are wider than the real samples' peaks.

III. Conclusions and Future Research

The goal of this thesis is to perform computational investigation of gold and silver nanotoroids, which are organized in finite arrays. Then, optical characterization of infinite gold nanotoroid arrays is performed to observe some difference between simulation and experimental situation. To have enough reliable information to create a model of those nanotoroids, there are some factors that the performer also needs to study such as the parameters of those frequency dependent materials, the surface resolution and reduction of computational domain by applying appropriate boundary conditions.

In this thesis, the Lorentz-Drude models for gold and silver are studied. After computing by Matlab, the results are different from the experimental data from Palik [3]'s, when it comes to high frequency. However, the desire range that the thesis looks at is from 450 to 850 nm, and in that range, the Lorentz-Drude models have the same result with the experimental data. Moreover, after convergence study with HFSS on an object of a gold sphere dimer with a radius of 40nm and a gap of 1nm, a surface approximation of 0.02 nm which provides an accurate result in acceptable computation time is used for all simulations. In addition, in order to reduce computation time and memory requirements by reduction of computational domain, the appropriate boundary conditions are studied and applied. In fact, the E symmetry boundary is applied on the plane to which vectors of electric field are perpendicular, while the H symmetry boundary is applied on the plane to which vectors of electric field are parallel. In addition, in the model of infinite arrays, the face-to-face settings of the same kind symmetry boundaries are applied to acquire reduction of computational domain.

For experimental study, some nanotoroids are chosen to be fabricated as arrays on the glass substrate and optical characterized by ellipsometry's transmission measurement. These

nanotoroids have inner radii of 50nm, 60nm and 100nm, while the outer radius is 150nm. The resonant peaks that are obtained by simulation appear at some frequencies that are close to the ones obtained by ellipsometry's measurement on fabricated samples. From this study, there is the observation that the glass substrate shifts the resonant wavelength to the high frequency spectrum.

Future work is to further study ellipsometry optical characterization. In fact, the optical properties of materials have an important role in modeling of some solar devices. Optical characterization not only helps to obtain material properties, but it also helps to create some theoretical model based on practical data.

Reference

[1] ANSYS, Inc.. <u>User's Guide – HFSS Online Help</u>. Pennsylvania: ANSYS, Inc., 2005.

[2] D. Swanson, Jr. and W. Hoefer, "Finite Element Method Simulators," in *Microwave Circuit Modeling Using Electromagnetic Field Simulation*. Boston: Artech House, 2003, ch. 6, pp. 125 – 127.

[3] E. Palik, Handbook of Optical Constants of Solids, New York: Academic, 1985.

[4] J. Hoffmann, C. Hafner, P. Leidenberger, J. Hesselbarth, and S. Burger. "Comparison of Electromagnetic Field Solvers for 3D Analysis of Plasmonic Nano Antennas," *Proc. SPIE,* vol. 7390, pp. 73900J-73900J-11,2009.

[5] N. Burford, "Plasmonic Nanostructures for the Absorption Enhancement of Silicon Solar Cells," M.S thesis, ELEG Dept., UARK Univ., Fayetteville, AR, 2013.

[6] S. Lim, W. Mar, P. Matheu, D. Derkacs, E. Yu, "Photocurrent Spectroscopy of Optical Absorption Enhancement in Silicon Photodiodes via Scattering from Surface Plasmon Polaritons in Gold Nanoparticles," *J. Appl. Phys.,* vol. 101, no. 104309, pp. 1-7, May 2007.

[7] A. Mary, D. M. Koller, A. Hohenau, J. R. Krenn, A. Bouhelier, A. Dereux, "Optical Absorption of Torus-Shaped Metal Nanoparticles in the Visible Range," *Phys. Rev. B,* vol. 76, pp. 245422-(1)-245422-(5), 2007.

[8] N. Burford and M. El-Shenawee, "Absorption Enhancement in Silicon Solar Cells due to Surface Plasmons of Nanoparticles," *Proc. of the IEEE int. Symp. on Antennas and Prop., 2012.*

[9] J.A. Woollam Co., Inc. <u>WVASE Manual</u>. Nebraska: J.A. Woollam Co., Inc.,2010.

[10] M. El-Shenawee, P. Blake, A. M. Hassan, and D. K. Roper, "Surface Plasmons of Finite Nanoring Arrays," Proceedings of the IEEE International Symposium on Antennas and Propagation and USNC/URSI National Radio Science Meeting, Spokane, WA, USA, pp. 1609-1612, J .

[11] M. El-Shenawee, "Polarization Dependence of Plasmonic Nanotoroid Dimer Antenna," IEEE Antennas and Wireless Propagation Letters, vol. 9, pp. 463-466, 2010. uly 3-8, 2011.

[12] A. Rakic, A. Djurisic, J. Elazar, and M. Majewski, "Optical properties of metallic films for vertical-cavity optoelectronic devices," *Applied Optics*, vol. 37, no.22, 1998.

[13] D. Pozar, "Electromagnetic Theory," in *Microwave Engineering,* 4th Ed. Massachusetts: John Wiley & Sons, Inc. , 2012, ch. 1, pp. 1 – 42.

[14] D. Weber and A. Pucci, "Antenna Interaction in the Infrared," in *Nanoantenna: Plasmon-Enhanced Spectroscopies for Biotechnological Applications,* vol. 1, M.L. Chapelle and A. Pucci, Eds. Danvers, MA: Pan Stanford, 2013, ch. 6, pp. 175-187.

[15] M. Mishchenko, L. D. Travis and A. Lacis, "" in *Scattering, Absorption, and Emission of Light by Small Particles*. New York: Cambridge University Press, 2004, ch. 6, sec. 6.6, pp. 201-202.

[16] N. Burford and M. El-Shenawee, "Optimization of Nanotoroid Arrays for Plasmonic Solar Cell Applications, " *Proc. of the IEEE int. Symp. On Antennas and Prop. and USNC/URSI National Radio Science Meeting, Orlando, USA, July 7, 2013.*

Appendix A: Matlab Code

```matlab
%% Lorentz-Drude Model for Gold

omega_p = 9.03;

f = [0.760; 0.024; 0.010; 0.071; 0.601; 4.384];

omega_k = [0; 0.415; 0.830; 2.969; 4.304; 13.32];

gamma = [0.053; 0.241; 0.345; 0.870; 2.494; 2.214];

freq = xlsread('freq.xlsx');

h = 4.135667516E-15;

omega = h*freq;

numerator = f*(omega_p)^2;

epsilon = 1 + numerator(1) ./(omega_k(1)^2- omega.^2 + 1i*omega*gamma(1)) ...

    + numerator(2) ./(omega_k(2)^2- omega.^2 + 1i*omega*gamma(2)) ...

    + numerator(3) ./(omega_k(3)^2- omega.^2 + 1i*omega*gamma(3)) ...

    + numerator(4) ./(omega_k(4)^2- omega.^2 + 1i*omega*gamma(4)) ...

    + numerator(5) ./(omega_k(5)^2- omega.^2 + 1i*omega*gamma(5)) ...

    + numerator(6) ./(omega_k(6)^2- omega.^2 + 1i*omega*gamma(6));

Au_e_real = real(epsilon);

Au_e_img = imag(epsilon);

Au_loss_tang = -Au_e_img./Au_e_real;

xlswrite('Gold.xlsx', [freq, Au_e_real, Au_loss_tang]);


%% Lorentz-Drude Model for Silver

omega_p = 9.01;

f = [0.845; 0.065; 0.124; 0.011; 0.840; 5.646];

omega_k = [0; 0.816; 4.481; 8.185; 9.083; 20.29];

gamma = [0.048; 3.886; 0.452; 0.065; 0.916; 2.419];

freq = xlsread('freq1.xlsx');

h = 4.135667516E-15;
```

```matlab
omega = h*freq;

numerator = f*(omega_p)^2;

epsilon = 1 + numerator(1) ./(omega_k(1)^2- omega.^2 + 1i*omega*gamma(1)) ...

    + numerator(2) ./(omega_k(2)^2- omega.^2 + 1i*omega*gamma(2)) ...

    + numerator(3) ./(omega_k(3)^2- omega.^2 + 1i*omega*gamma(3)) ...

    + numerator(4) ./(omega_k(4)^2- omega.^2 + 1i*omega*gamma(4)) ...

    + numerator(5) ./(omega_k(5)^2- omega.^2 + 1i*omega*gamma(5)) ...

    + numerator(6) ./(omega_k(6)^2- omega.^2 + 1i*omega*gamma(6));

Ag_e_real = real(epsilon);

Ag_e_img = imag(epsilon);

Ag_loss_tang = -Ag_e_img./Ag_e_real;

xlswrite('Silver.xlsx', [freq, Ag_e_real, Ag_loss_tang]);
```